# Adaptive Quasi-static Modelling of Needle Deflection During Steering in Soft Tissue

Carlos Rossa[1], Mohsen Khadem[1], Ronald Sloboda[2], Nawaid Usmani[2], and Mahdi Tavakoli[1]

***Abstract*— In this paper we present a model for needle deflection estimation in soft tissue. The needle is modelled as a vibrating compliant cantilever beam that experiences forces applied by the tissue as it is inserted. Each of the assumed vibration modes are associated with a weighting coefficient whose magnitude is calculated using the minimum potential energy method. The model only requires as input the tissue stiffness and needle-tissue cutting force. Contributions of this paper include the estimation of needle-tissue contact forces as a function of the tissue displacement along the needle shaft, while allowing for multiple bends of the needle. The model is combined with partial ultrasound image feedback in order to adaptively calculate the needle-tissue cutting force as the needle is inserted. The image feedback is obtained by an ultrasound probe that follows the needle tip and stops at an appropriate position to avoid further tissue displacement. Images obtained during early stages of the insertion are used to predict the deflection of the needle further along the insertion process. Experimental results in biological and phantom tissue show an average error in predicting needle deflection of 0.36 mm.***

***Index Terms*— Medical robots and systems, steerable needles, quasi-static modelling, needle-tissue interaction, needle deflection.***

## 1. MOTIVATION

Needle insertion is an essential component of several clinical interventions such as biopsies, radio frequency ablation, neurosurgery, drug delivery, and brachytherapy cancer treatment. Accurate guidance of the needle tip towards a clinical target is a decisive factor in the success of these procedures. Inaccurate needle placement may limit the effectiveness of the treatment or lead to undesirable side effects. Controlling the trajectory of flexible needles within soft tissue is challenging because, in practice, intrinsic needle-tissue interaction causes the needle to bend, which in turn deforms body tissues and targets [1]. Bevelled-tip needles are often used for percutaneous insertions as the needle tip can easily cut and penetrate a soft tissue. As the bevel cuts the tissue, an imbalance of forces is generated at the needle tip leading the needle to deflect from a straight path [2].

Solutions to mitigate needle targeting errors are often sought in physically modelling the needle-tissue interaction in order to estimate the needle deflection and carry out the necessary corrective actions. The simplest model that captures needle deflection during insertion is the nonholonomic model [3]. The needle tip is assumed to follow a circular path whose curvature and direction of deflection can be controlled by rotating the needle base around the needle shaft [4]. The tissue is considered to be stiff relative to the needle as the model cannot account for tissue deformation. In practice, this assumption does not hold as tissue deformation does occur due to needle deflection [5]. In fact, needle deflection and tissue deformation are coupled effects that influence each other [6].

To account for tissue deformation, mechanics-based models have been extensively used to model needle insertion into soft tissue [7], [8], [9]. In these methods, different assumptions are made to model the resulting needle-tissue contact force profiles such as that of distributed loads along the needle shaft [10], or forces being proportional to tissue deformation [1], [11]. More complex models of tissue deformation have been developed using finite element methods [12], [13] that can account for the effects of needle rotation.

Typically, physical models require as input several hard-to-characterize properties of the needle-tissue interaction. This input information is difficult to obtain and not always available from in-vivo procedures. In addition, most models can only account for a fixed set of inputs that cannot be updated during the insertion procedure. Although model parameter identification is unavoidable when employing physical models, limiting the number of parameters to those that can be identified during the procedure could facilitate the implementation of the model in clinical practice.

Besides using needle-tissue modelling for estimating needle deflection, medical imaging techniques such as ultrasound are commonly used to directly monitor the needle and target position during insertion [14], [15]. Biomechanical models of needle in tissue and image-based needle tracking techniques turn out to be complementary. Accurate measurements of needle position can be fed into physical models to continuously update model parameters [16], [17], [18]. For instance, in [19] ultrasound images of the needle tip are used to calculate the actual curvature followed by the needle tip and update a needle steering controller. In [20] deflection models and image feedback are integrated to guide the needle towards a moving target. Tracking the needle tip in ultrasound images during insertion requires the probe to move in synchrony with the

[1]Carlos Rossa, Mohsen Khadem, and Mahdi Tavakoli are with the Department of Electrical and Computer Engineering, University of Alberta, AB, Canada T6G 2V4. E-mail: rossa@ualberta.ca; mohsen.khadem@ualberta.ca; madhi.tavakoli@ualberta.ca.

[2]Ron Sloboda and Nawaid Usmani are with the Cross Cancer Institute and the Department of Oncology, University of Alberta, Edmonton, AB, Canada T6G 1Z2. E-mail: {ron.sloboda, nawaid.usmani}@albertahealthservices.ca.

needle [4], [21]. Probe motion during the clinical procedure can result in unwanted deformation of the surrounding tissue which may result in anatomic variations of the pre-operatively planned needle target location [22]. Thus, limiting the motion of the ultrasound probe is desirable to avoid discrepancies between pre-and intra-operative locations of clinical targets.

The motivation of this paper is to propose a model for needle deflection estimation with a limited number of parameters. The needle is modelled as a vibrating compliant cantilever beam that undergoes forces applied by the tissue as it is inserted. Each of the assumed vibration modes is associated with a weighting coefficient whose magnitude is calculated as a function of the model parameters. The model only requires as input the tissue stiffness and the tissue cutting force. Contributions of this paper include: (1) a novel tissue model that estimates tissue deformation and the resulting needle-tissue contact forces along the shaft while allowing for multiple bends of the needle; (2) a closed form approach for estimating needle deflection that makes the model computationally efficient; and (3) a method to update needle-tissue cutting force on the fly from partial ultrasound image feedback, where the ultrasound probe follows the needle tip and stops at an appropriate position to minimize tissue deformation.

The rest of the paper is organized as follows. In the next section we introduce the needle-tissue model and a variational method used to solve it, and describe how image feedback can be used to update the model parameters. Section 3 presents the needle insertion setup used for validating the proposed method. Validation of the proposed method in biological *ex-vivo* and phantom tissues reported in Section 4 shows an average maximum error in predicting needle deflection of 1.2 mm with an mean error of 0.36 mm.

## 2. NEEDLE-TISSUE INTERACTION MODEL

Regardless of how the needle interacts with the tissue, the needle can be modelled as a cantilever beam that experiences forces applied by the tissue. The deflection of a beam can be approximated as the sum of $n$ admissible deflection functions representing the first $n$ modes of vibration, each of which is multiplied by an unknown weighting coefficient [7]. The deflection functions are trial beam shape functions that must satisfy the boundary conditions of a cantilever beam and be differentiable at least up to the highest order of the partial differential equations of the beam. The deflection $v(d, z)$ of beam can be defined as

$$v(d,z) = \sum_{i=0}^{n} q_i(z)g_i(d) \tag{1}$$

where $q_i(z)$ gives the displacement of the beam at each point $z$ along its shaft and $g_i(d)$ is a weighting coefficient for each of the vibration modes with $d$ being the current insertion depth. The eigenfunctions $q_i(z)$ for a cantilever beam of length $L$ normalized in such a way that the maximum displacement (deflection) is equal to unity, is given by [23]

$$q_i(z) = \frac{1}{\kappa_i}\left[\sin(\beta_i \frac{z}{L}) - \sinh(\beta_i \frac{z}{L}) - \gamma_i\left\{\cos(\beta_i \frac{z}{L}) - \cosh(\beta_i \frac{z}{L})\right\}\right] \tag{2}$$



(a) Forces acting on the needle during insertion



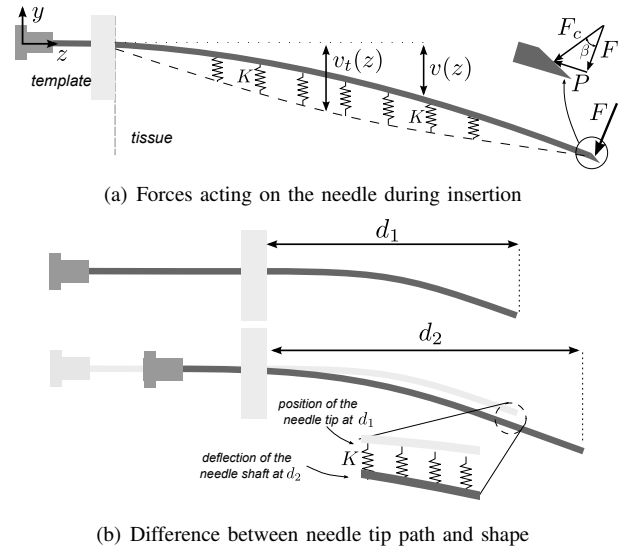(b) Difference between needle tip path and shape

Fig. 1. Needle insertion in soft tissue. As the needle cuts a path in the tissue, a force $F_c$ is applied to the needle tip causing the needle to bend. $F$ and $P$ are the transverse and longitudinal components of $F_c$, respectively, that depend on the needle bevel angle $\beta$. Tissue compression resulting the needle bending is assumed to be the difference between the current shape of the needle $v(z)$ and the path cut by the needle tip $v_t(z)$.

where the constants $\gamma_i$ and $\kappa_i$ are computed as

$$\gamma_i = \frac{\sin\beta_i + \sinh\beta_i}{\cos\beta_i + \cosh\beta_i} \tag{3}$$
$$\kappa_i = \sin\beta_i - \sinh\beta_i - \gamma_i(\cos\beta_i - \cosh\beta_i).$$

The values of the constants $\beta_i$ for a cantilever beam (clamped-free) are $\beta_1 = 1.857$, $\beta_2 = 4.695$, $\beta_3 = 7.855$, $\beta_4 = 10.996$, and $\beta_i \simeq \pi(i - 1/2)$ for $i > 4$ [23]. At this stage the assumed displacement functions are entirely parametrized. In the following, we shall see that the weighting coefficients $g_i(d)$ can be calculated as a function of the needle-tissue interaction forces such that the system reaches equilibrium.

### 2.1 Needle-Tissue Equilibrium

To find the needle deflection given in (1), we need to calculate the weighting coefficients $g_i(d)$ that satisfy the equilibrium of the coupled needle-tissue system. To this end, we will use a variational method known as the Rayleigh-Ritz method in which equilibrium of the system is established using the principle of minimum potential energy. This approach has been previously used to estimate needle deflection in [9], [20]. An important difference of our model compared to [9], [20] is a new tissue model that allows for an unlimited number of needle rotations while accounting for tissue deformation. Another contribution of this work is closed-form model parameter estimation from partial ultrasound image observation. We propose an approach to reduce the model to a simple system of linear equations that make it computationally efficient.

The coefficients $g_i(d)$ are those that minimize the system potential $\Pi(d)$ defined by

$$\Pi(d) = U(d) + V(d) \tag{4}$$

where $U(d)$ is the total stored energy in the system and $V(d)$ is the work done by conservative forces. Let us now derive the expressions for the potential energy and the work for the needle-tissue system.

Consider a needle of length $L$ being inserted into a tissue as shown in Fig. 1(a). As the needle tip cuts through the tissue, a reaction force $F_c$, known as the cutting force, is applied at the needle tip perpendicular to the bevel angle and causes the needle to bend. This force can be decomposed into a longitudinal and a transverse components (see the needle tip in Fig. 1(a)). We will neglect the effects of the longitudinal component of $F_c$ as it mostly induces axial compression of the needle. For small deflections, the transverse force $F$ is given by $F = F_c \cos(\beta)$, where $\beta$ is the needle bevel angle. As the needle bends, the work due to $F$ is computed as

$$V(d) = -Fv(d,L). \tag{5}$$

which will contribute to $\Pi(d)$ in (4). As a result of the needle deflection, the bending strain energy stored in the needle is

$$U_b(d) = \frac{1}{2} \int_0^L EI \left( \frac{\partial^2 v(d,z)}{\partial z^2} \right)^2 dz, \tag{6}$$

where $E$ and $I$ are the needle Young's modulus of elasticity and its second moment of inertia, respectively.

In some needle insertion procedures, such as in prostate brachytherapy, a guiding template is used to minimize the needle deflection outside the tissue and to help guide the needle towards a target location. We model the template as a rigid spring of stiffness $K_p >> 0$ with no thickness, that is connected to the needle shaft at a distance of $z_t$ from the needle's base with $z_t = L - d - c_t$, where $c_t$ is the distance from the template to the tissue surface (see Fig. 1(a)). The potential energy stored in the template is

$$U_p(d) = \frac{1}{2} K_p v(d, z_t)^2. \tag{7}$$

If the template is not used, $K_p$ must be set to zero.

As the needle bends, it deforms the surrounding tissue which in turn applies forces to the needle. Assuming small local magnitude and deformation velocity of the tissue, it is reasonable to assume that the tissue is a purely elastic medium. Thus, the force applied to the needle at a certain point along the shaft becomes proportional to the tissue displacement at that point. If we call $v_t(z)$ the initial position of the undeformed tissue, the tissue reaction force is $K(v(d,z) - v_t(z))$ (see Fig. 1(a)), where $K$ is the stiffness of the tissue. Now, modelling the tissue is simply a matter of defining $v_t(z)$.

The assumption here is that tissue displacement is equal to the difference between the current position of the needle shaft and the previous path that was cut by the needle tip. An example is shown in Fig. 1(b). The needle is first inserted to a depth of $d_1$ and then advanced by $\tau$ to reach a depth of $d_2$. The deflection of the needle tip when it was inserted to $d_1$ was $v(d_1, L)$ and the current deflection of the shaft at the position the tip was at $d_1$ is $v(d_2, L - \tau)$. For a generic point along the shaft, one defines the equilibrium position of the tissue as $v_t(z) = v(d - \tau, L)$. Therefore, the energy due to

tissue compression is given by

$$U_t(d) = \frac{1}{2} K \int_{L-d}^L [v(d,z) - v(d-\tau, L)]^2 dz. \tag{8}$$

Notice that as the new proposed tissue model essentially compares the current needle shape with the path cut by the needle tip, it allows for an unlimited number of needle rotations. Now that we have defined all the energies and the work in the system, we can calculate the eigenvalues $g_i(d)$ using the minimum potential energy principle. According to the Rayleigh-Ritz method [24], the coefficients $g_i(d)$ must give $\delta \Pi_i = 0$ for any values of $\delta g_i$ where $\delta$ denotes an infinitesimal difference. Thus, minimizing the system potential with respect to the unknown $g_i(d)$ is equivalent to setting the variation in the potential with respect to the coefficients equal to zero. Therefore, one can state:

$$\delta \Pi_i(d) = \frac{\partial}{\partial g_i(d)} (U_b + U_p + U_t + V) \partial g_i(d) = 0. \tag{9}$$

Inserting the equations of the energies (6)-(8), and of the work (5) in (9) to solve for $g_i(d)$ yields:

$$\frac{\partial}{\partial g_i(d)} \left( \frac{EI}{2} \int_0^L \left[ \frac{\partial^2}{\partial z^2} \sum_{i=1}^n q_i(z) g_i(d) \right]^2 dz \right.$$
$$+ \frac{K}{2} \int_{L-d}^L \left[ \sum_{i=1}^n q_i(z) g_i(d) - \sum_{i=1}^n q_i(L) g_i(d-\tau) \right]^2 dz$$
$$\left. + \frac{K_p}{2} \left[ \sum_{i=1}^n q_i(z_t) g_i(d) \right]^2 - F \sum_{i=1}^n q_i(L) g_i(d) \right) = 0. \tag{10}$$

Taking the partial derivative with respect to $g_i(d)$, and knowing that $q_i(L) = 1$, results in

$$EI \int_0^L \left( \sum_{i=1}^n \ddot{q}_i(z) g_i(d) \right) \ddot{q}_i(z) dz + K_p \left( \sum_{i=1}^n q_i(z_t) g_i(d) \right) q_i(z_t)$$
$$+ K \int_{L-d}^L \left( \sum_{i=1}^n q_i(z) g_i(d) \right) q_i(z) dz \tag{11}$$
$$- K \int_{L-d}^L \left( \sum_{i=1}^n g_i(d-\tau) \right) q_i(z) dz = F,$$

where the double dot denotes the second derivative with respect to $z$. Expanding the summations allows to write the first three terms only as functions of $z$. For instance, the first term can be rewritten as:

$$EI \left( g_1(d) \int_0^L \ddot{q}_1(z) \ddot{q}_i(z) dz + g_2(d) \int_0^L \ddot{q}_2(z) \ddot{q}_i(z) dz \right.$$
$$\left. \cdots + g_n(d) \int_0^L \ddot{q}_n(z) \ddot{q}_i(z) dz \right). \tag{12}$$

Thus, by creating four new variables that we define as

$$\Psi_{ji} = \int_0^L \ddot{q}_i(z)\ddot{q}_j(z)dz, \qquad \Omega_{ji} = \int_{L-d}^L q_i(z)q_j(z)dz,$$

$$\Gamma_{ji} = q_i(z_t)q_j(z_t), \qquad \phi_{ji} = \int_{L-d}^L g_j(d-\tau)q_i(z)dz, \qquad (13)$$

(11) can be rearranged as follows

$$\sum_{j=1}^n \left[ g_j(d)(EI\Psi_{ji} + K\Omega_{ji} + K_p\Gamma_{ji}) - K\phi_{ji} \right] = F, \qquad (14)$$

with $\Psi_{ji}$, $\Omega_{ji}$, and $\Gamma_{ji}$ being only functions of $z$ and therefore can be solved easily. Special attention must be given to the last integral in (11) as it has a delay term $\tau$. Thus, $\phi_{ji}$ in (13) is also a function of $g(d)$. In the following, we will convert $\phi_{ji}$ into a convolution form in order to eliminate the delay.

*2.2 Model Simplification*

In the last integral of (13) that defines $\phi_{ji}$, the weighing coefficient $g_i$ is delayed from $d$ by $\tau = L - z$. To eliminate the delay, it is convenient to take the integral of a delayed function over its delay term. Using a simple change of variable, i.e., $z = L - \tau$, results in

$$\phi_{ji} = \int_0^d g_j(d-\tau)q_i(\tau)d\tau \qquad (15)$$

where, according to (2), $q_i(\tau)$ is computed as

$$q_i(\tau) = \frac{1}{\kappa_i} \left[ \sin(\lambda_i\tau + \beta_i) - \sinh(\lambda_i\tau + \beta_i) + \right.$$
$$\left. - \gamma_i(\cos(\lambda_i\tau + \beta_i) - \cosh(\lambda_i\tau + \beta_i)) \right], \qquad (16)$$

with $\lambda_i = \beta_i/L$. Close scrutiny of (15) indicates that we have transformed the delayed function $\phi_{ji}$ into a convolution integral. Applying the Laplace transform to $\phi_{ji}$ over $d$ yields

$$\mathscr{L}\{\phi_{ji}(d)\} = \Phi_{ji}(s) = G_j(s)Q_i(s), \qquad (17)$$

where $Q_i(s) = \mathscr{L}\{q_i(\tau)\}$ with $q_i(\tau)$ given in (16). Hence, expanding the previous equation gives

$$\Phi_{ji}(s) = \frac{G_j(s)}{\kappa_j} \left[ \frac{s(\sin\beta_i) + \lambda_i\cos\beta_i}{s^2 + \lambda_i^2} - \frac{\lambda_i\cosh\beta_i + s\sinh\beta_i}{s^2 - \lambda_i^2} \right.$$
$$\left. - \gamma_i \left( \frac{s(\cos\beta_i) - \lambda_i\sin\beta_i}{s^2 + \lambda_i^2} - \frac{s(\cosh\beta_i) + \lambda_i\sinh\beta_i}{s^2 - \lambda_i^2} \right) \right]. \quad (18)$$

Applying the inverse Laplace transform on both sides of the previous equation results in:

$$(\phi_{ji}^{''''} - \lambda_i^4\phi_{ji})\kappa_j = \kappa_i g_j^{'''}(d) + a_i g_j^{''}(d) + b_i g_j(d), \qquad (19)$$

where the prime denotes the derivative with respect to $d$. The constants $a_i$, and $b_i$ are

$$a_i = \lambda_i[\cos\beta_i - \cosh\beta_i + \gamma_i(\sin\beta_i + \sinh\beta_i)]$$
$$b_i = \lambda_i^3[\cos\beta_i - \cosh\beta_i - \gamma_i(\sin\beta_i - \sinh\beta_i)]. \qquad (20)$$

As we can note, the delay term has vanished and $\phi_{ji}$ can be shown to satisfy (19).

Now, in order to find the weighting coefficients $g_i(d)$, one writes $n$ equations (14), one for each of the assumed vibration modes. The weighting coefficients are simply found by solving the system of $n$ linear equations given in (21). Notice that $\Psi_{ij} = \Psi_{ji}$, $\Omega_{ij} = \Omega_{ji}$, $\Gamma_{ij} = \Gamma_{ji}$, and $\phi_{ij} = \phi_{ji}$.

$$\begin{bmatrix} g_1(d) \\ g_2(d) \\ \vdots \\ g_n(d) \end{bmatrix} \begin{bmatrix} EI\Psi_{11} + K\Omega_{11} + K_p\Gamma_{11} & EI\Psi_{12} + K\Omega_{12} + K_p\Gamma_{12} & \dots & EI\Psi_{1n} + K\Omega_{1n} + K_p\Gamma_{1n} \\ EI\Psi_{12} + K\Omega_{12} + K_p\Gamma_{12} & EI\Psi_{22} + K\Omega_{22} + K_p\Gamma_{22} & & EI\Psi_{2n} + K\Omega_{2n} + K_p\Gamma_{21} \\ \vdots & & \ddots & \vdots \\ EI\Psi_{1n} + K\Omega_{1n} + K_p\Gamma_{1n} & EI\Psi_{2n} + K\Omega_{2n} + K_p\Gamma_{2n} & \dots & EI\Psi_{nn} + K\Omega_{nn} + K_p\Gamma_{nn} \end{bmatrix} - K \begin{bmatrix} \phi_{11} & \phi_{12} & \dots & \phi_{1n} \\ \phi_{12} & \phi_{22} & & \phi_{2n} \\ \vdots & & \ddots & \vdots \\ \phi_{1n} & \phi_{2n} & \dots & \phi_{nn} \end{bmatrix} = F \qquad (21)$$

*2.3 Model Parametrization Using Image Feedback*

The proposed model requires as input the force at the needle tip and the tissue stiffness. This parameters are not always available to in operating room conditions. However, in an *in vivo* procedure, tissue Young's modulus can be estimated using an ultrasound-based Acoustic Radiation Force Impulse (ARFI) imaging technique that relates the shear wave propagation speed of the ultrasound probe to the mechanical properties of the tissue (see [19]). Then, the tissue stiffness can be derived from the measured Young's modulus. Measuring the needle-tissue cutting force is a much more challenging task. Here, we propose a closed-form approach to estimate the cutting force using only partial image feedback of the needle during insertion. This is another contribution if this paper and has

many practical uses.

Let us assume that the deflection of the needle tip can be acquired from image feedback and is called $v_0$. Thus, from (1) we can write:

$$v(L, d) = g_1(d) + g_2(d) + \dots g_n(d) = v_0. \qquad (22)$$

Now, let us add this equation to the system of $n$ equations given in (21) such that we get a system of $n + 1$ independent expressions with only $n$ unknown parameters. Therefore, one can solve for the tip force using the extended system of equations when image feedback is available. The description of how the needle deflection is measured in ultrasound images can be found in [14]. Note that position feedback of the needle could be obtained from another imaging or sensing modality.
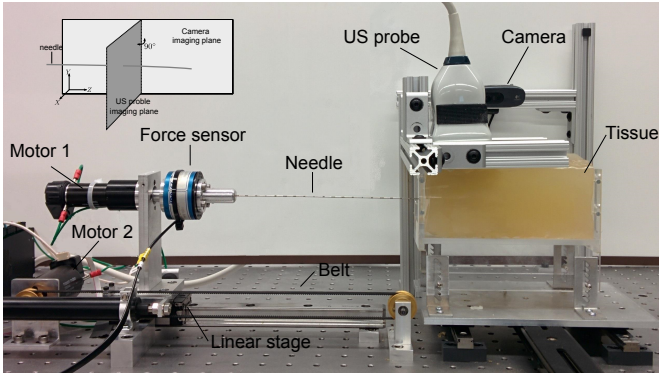
Fig. 2. 2 DOF needle insertion robot. A motor provides the linear motion to insert the needle into the phantom tissue. A second motor attached to the needle rotates it around its shaft. The axial force (along $Z$) at the needle base is measured by a force sensor. Images of the needle inside tissue are recorded by a camera in the $(Y, Z)$ plane by an ultrasound probe in the $(X, Y)$ plane. The ultrasound probe is mounted on a second linear stage (not visible) that is controlled such that the ultrasound imaging plane always contains the needle tip.

## 3. EXPERIMENTAL SETUP

Fig. 2 shows the two-degrees-of-freedom robotic system used for conducting needle insertion experiments in soft tissue. A 6-DOF force/torque sensor (JR3, Inc. Woodland, USA) is connected to the needle base and measures the axial insertion force (the other 5-DOF of force/torque sensing are not used). A RE-25 Maxon motor can rotate the needle around its shaft. The assembly can translate thanks to a linear stage actuated by a RE-40 Maxon motor through a belt and pulley mechanism.

Validation of the proposed method in this paper is performed using camera and ultrasound images to measure the needle deflection in semitransparent and biological phantoms respectively. A camera records at 30 Hz images of the needle inside a semitransparent tissue from the side of the tissue container (in the $(Y, Z)$ plane defined in the upper left corner of Fig. 2). The needle is steered such that its deflection plane is parallel to the camera imaging plane. The images are processed to output the needle shape in the form of a polynomial, from which the position of the needle tip is calculated given the needle insertion depth. The image processing algorithm used to measure the needle deflection in camera images can be found in [10].

For validation of the model in biological tissue, a 4DL14-5/38 Linear 4D ultrasound transducer connected to a Sonix-Touch ultrasound machine (Ultrasonix, Richmond, Canada) is placed above the tissue to acquire 2D images of the needle in the $(X, Y)$ plane shown in Fig. 2. The ultrasound probe is connected to a second motorized linear stage so that the position of the probe can be independently controlled (not visible in Fig. 2). The horizontal position of the probe is recorded by a linear potentiometer (Midori Precisions, Tokyo, Japan) and it is controlled such that the imaging plane always contains the needle tip. We use the method proposed in [14] to measure the needle deflection in ultrasound images. The needle appears as a bright spot along with extraneous background objects. To remove the majority of these objects we first define a region of interest (ROI) that limits the search for the needle

### TABLE I
#### FIXED MODEL PARAMETERS.

|  | Biological Tissue | Plastisol Tissue |  |  | Needle | Wire |
|---|---|---|---|---|---|---|
| K [kNm$^{-2}$] | 59.8 | 302.2 | | E [GPa] | 200 | 75 |
| $F_{5mm/s}$ [N] | 1.15 | 0.62 | | I [m$^4$10$^{-13}$] | 77.5 | 1.96 |
| $F_{30mm/s}$ [N] | 1.20 | 0.71 | | L [mm] | 200 | 180 |

to a small section of the image. The ROI consists of a square with a width of 5 times the needle radius. In frame $f$, the ROI is centred around the position of the needle found in frame $f - 1$. Therefore, as the needle moves transversely in successive ultrasound images, the ROI moves accordingly such that the needle will always be located in the ROI. The Matlab function *imadjust* applies an intensity transformation to the image to improve the visibility of bright points. Next, we use an intensity threshold to obtain a set of candidate pixels for the needle within the axial image. Finally, a Kalman filter is used to predict where the needle should be within the ROI given the needle's historical trajectory. When image feedback is used in the model for on-line identification of model parameters, the obtained needle tip deflection is inserted in (22).

Two different needles are used in our experiments. Needle 1 is a 200 mm long standard 18-gauge brachytherapy needle (Eckert & Ziegler Inc., Oxford, USA) which has a Young's modulus of 200 GPa, a moment of inertia of $7.75 \times 10^{-14}$ m$^4$, and a tip bevel angle of 20 degrees. Needle 2 is a 180 mm Nitinol wire (Kellogg's Research Labs, Plymouth, USA) which is inserted into a 5 mm long tip of needle 1 and fixed in place with adhesive. The wire's Young's modulus of elasticity is 75 GPa and its second moment of inertia is $1.96 \times 10^{-13}$ m$^4$. The grid template is assumed to have a stiffness of $K_p = 10^9$ N/m.

Needle insertion experiments are performed in two different soft tissue samples with distinct mechanical properties. Tissue 1 is prepared by embedding a piece of beef tenderloin in an industrial gelatin preparation derived from acid-cured tissue (gel strength 300 from Sigma-Aldrich Corporation, Saint Louis, USA). Tissue 1 presents several layers of fat and some muscles, making it highly non-homogeneous. The gelatin is meant to create a flat surface to ensure good acoustic contact between the ultrasound probe and the biological tissue. The needle is only inserted in the latter and never goes through the gelatin.

Tissue 2 is prepared with plastisol gel (M-F Manufacturing Co., Fort Worth, USA). We use this plastisol tissue to test the proposed method in an environment with high friction coefficient. The needle-tissue viscous friction coefficient in Tissue 2 is four times higher than in Tissue 1. The amount of added plastic softener in the mixture determines the stiffness of the tissue sample. We use a concentration ratio of 80% of liquid plastic and 20% of softener.

The only tissue parameters required in the deflection model are the tissue stiffness and the force applied at the needle tip. Similarly to [9], we estimate the force applied at the needle tip during insertion (i.e., $F_c$ and $F$) by measuring the axial force at the base of a shortened needle when it slices through a thin tissue sample. As the needle tip penetrates the tissue, the
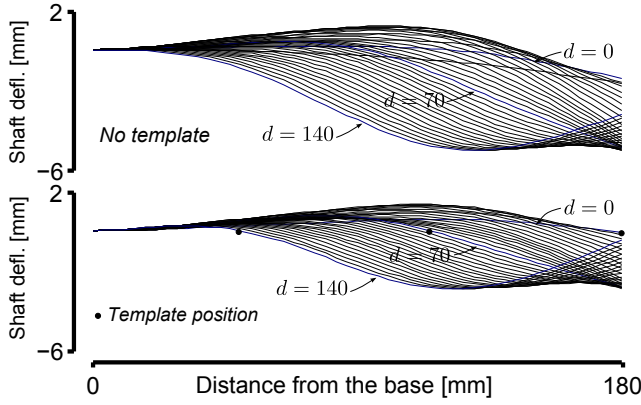
Fig. 3. Model predicted shape of the wire as it is inserted in plastisol. The plot shows the influence of the guiding template on the deflection when the wire is rotated at 80 mm. Each line corresponds to the needle shape at a given insertion depth $d$ (deflection of a needle shaft point versus its distance from the base). In the second plot, the dot indicates the position of the template along the shaft.

TABLE II

AVERAGE MAXIMUM AND AVERAGE MEAN ERROR IN PREDICTING NEEDLE TIP DEFLECTION. UNITS ARE IN MILLIMETRES.

| Tissue | | Rotation depth | Maximum error | Standard deviation | Mean error | Standard Deviation |
|---|---|---|---|---|---|---|
| 1 | (5 mm/s) | - | 0.992 | 0.094 | 0.242 | 0.053 |
| 1 | (30 mm/s) | - | 1.185 | 0.224 | 0.293 | 0.045 |
| 1 | (5 mm/s) | 40 | 1.905 | 0.667 | 0.452 | 0.207 |
| 1 | (5 mm/s) | 80 | 1.053 | 0.307 | 0.203 | 0.065 |
| 1 | (5 mm/s) | 40&80 | 1.497 | 0.149 | 0.382 | 0.180 |
| 2 | (5 mm/s) | - | 0.839 | 0.329 | 0.332 | 0.167 |
| 2 | (5 mm/s-wire) | - | 1.130 | 0.197 | 0.654 | 0.147 |
| Average over 35 samples | | | 1.228 | | 0.365 | |

measured axial insertion force corresponds to the transverse component $P$ of the cutting force $F_c$ plus the frictional force generated along the shaft (see the zoomed needle tip in Fig. 1). Inertial effects are neglected due to the low constant insertion velocity. The insertion is carried on until the needle tip exits the tissue. Therefore the force applied at the tip becomes zero and the measured force $P$ corresponds to friction only. Thus, the axial component $P$ of the cutting force $F_c$ can be isolated by subtracting the measured friction from the total force. The transverse load $F$ is then calculated as $F = P\tan(\beta)^{-1}$ where $\beta = 20°$ is the tip bevel angle. Four different trials are performed for each tissue at 5 and 30 mm/s insertion velocity. The average measured values are summarized in Table I.

Finally, we performed relaxation tests to find the tissue stiffness $K$. The needle in the insertion setup is replaced with a flat indenter with a diameter of 3 mm. Then, the robot is controlled to apply a position step input to the indenter. The insertion robot moves the indenter to a fixed position and the indenter's displacement as well as the reaction force are recorded. The experiments are performed with a velocity of 10 mm/sec to indentation depths of 5, 8, and 10 mm. The average identified tissue stiffness is reported in Table I.

## 4. EXPERIMENTAL RESULTS

We will conduct experiments in two different scenarios. In the first scenario, the measured tissue stiffness and the cutting force are fed into the model to predict the needle tip deflection. No image feedback is used. In the second scenario, measured needle tip deflection in ultrasound images is used to update the needle-tissue cutting force as the needle is inserted. In both cases, the needle is initially inserted by 5 mm and then further inserted to a depth of 140 mm in the tissue.

The model predicted results in Fig. 3 show the influence of the guiding template on the needle shape as it is inserted and rotated at 80 mm in plastisol. The model can capture the effects of the template by minimizing the deflection of the needle outside the tissue.

The model predicted and the measured tip deflection of the needle and wire during insertion in plastisol are shown in Fig. 4(a). Insertions are performed at a constant velocity of 5 mm/s without axial rotation. Insertions involving the wire are performed using the guiding template. The error observed across 10 insertions remains below 2 mm. Results in biological tissue are shown in Fig. 4(b). The brachytherapy needle is inserted at two different velocities of 5 mm/s and 30 mm/s. The average maximum error in predicting needle tip deflection is 1.18 mm.

Experimental results involving axial rotation of the needle at an insertion depth of either 40 mm or 80 mm, as well as double rotation at 40 and 80 mm are shown in Fig. 5. In the model, upon rotation of the needle at a depth $d_r$, we progressively reverse the direction of the tip force: The tip force gradually decreases from $F$ at $d_r$ to reach $-F$ at $d_r + 5$ mm. From this point $F$ is kept constant until another rotation takes place. Since the needle shaft is pushed to stay close to the path cut by the needle tip, the model can simulate multiple rotations of the needle.

The average maximum error and average mean error in predicting needle tip deflection for each of the above described scenarios are summarized in Table. II. Overall, the average maximum error and the mean over 35 trials are 1.22 and 0.36 mm, respectively. This is a reasonable accuracy given the diameter of the needle and the measurement noise in present in ultrasound images. Although the model shows good performance in biological tissue, the mean error observed in high friction plastisol is twice as high. This was expected because the model neglects the effects of friction, which is highly dependent on insertion velocity.

The estimated tip force using this method is shown in Fig. 6(a) as a function of the insertion depth. In the biological tissue, the average of the estimated cutting force is 1.25 $\pm 0.245$ N which covers the measured value in the experiments described in Section 3 of 1.15 N. For the plastisol tissue, the estimated force is $0.72 \pm 0.352$ N and the measured force is 0.62 N.

As discussed in Section 1, it is suitable to limit the motion of the ultrasound probe in order to avoid tissue deformation. Hence, let us consider a case where the ultrasound probe follows the needle tip up to certain depth and then stops. Once the probe stops, we calculate the average of the estimate cutting force over the 5 mm of insertion that precede the stopping

(a) Plastisol tissue - needle and wire inserted at 5 mm/s

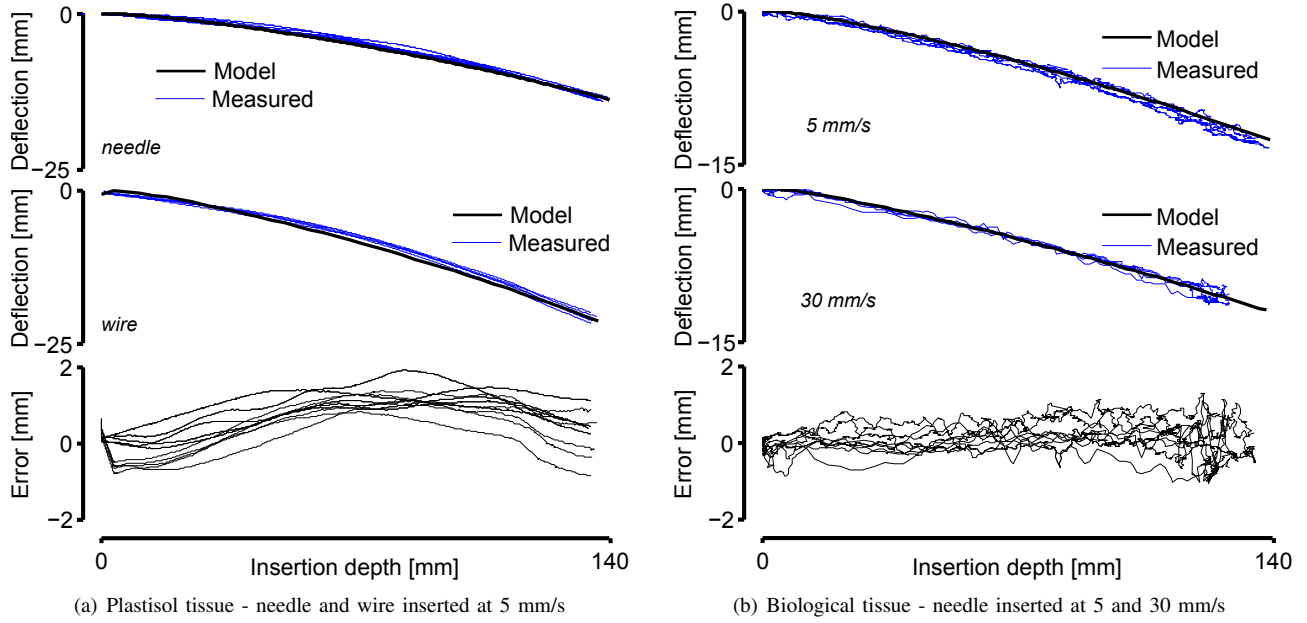(b) Biological tissue - needle inserted at 5 and 30 mm/s

Fig. 4. Experimental results in plastisol and biological tissue. The needle tip deflection measured from ultrasound images is compared to the predicted deflection using the proposed model. Five insertions are performed under different scenarios, i.e., needle and wire in plastisol (a), and needle inserted in biological tissue at different velocities (b).
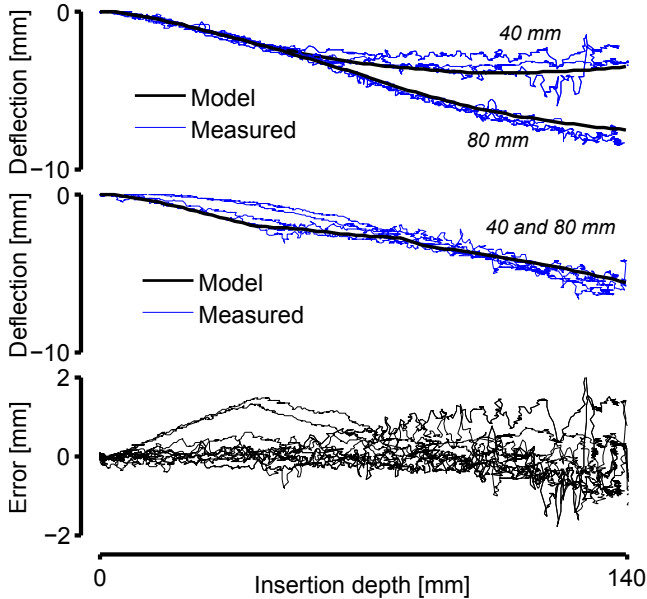


Fig. 5. Experimental results in biological tissue with axial needle rotation. In the upper plot the needle is rotated by $180°$ at a depth of either 40 or 80 mm. Double rotation at 40 and 80 mm is shown in the middle plot. For all the cases, the insertion velocity is 5 mm/s.

position. Using the averaged cutting force, we predict future deflections of the needle further along the insertion process. This is very useful in practical conditions as it allows to limit the motion of the ultrasound probe and minimize further tissue displacement. Fig. 6(b) shows the average maximum and mean error in predicting the deflection for 10 insertions in biological tissue (without needle rotation) as a function of the maximum depth of the ultrasound probe (stopping position). After 20 mm the model is able to correctly estimate the cutting force

as the maximum average error remains below 2 mm, and is reduced to less than 1 mm when the probe stops at or after 55 mm.

## 5. CONCLUSION

In this paper, we propose a method to estimate needle deflection based on the first four assumed vibration modes of a compliant cantilever beam. The needle is modelled as a vibrating structure that experiences forces applied by the tissue. Each vibration mode is associated with a weighting coefficient. Contributions of this paper include a tissue model that compares the actual needle shape with the path cut by the needle tip in order to calculate the contact force profile along the needle shaft. The model allows for multiple rotations of the needle during insertion. Experimental results in inhomogeneous biological tissue and plastisol showed an average maximum error in predicting needle tip deflection of 1.22 mm $\pm 0.28$ mm over 35 trials, and an average error of 0.36 mm. According to [19] this observed error remains in the range of the smallest tumour that can be detected by US images (2 mm).

With a limited number of model parameters, the proposed model shows a relatively good accuracy. For instance, the well-known nonholonomic [3] model reports an error between the model prediction and measurements of 1.3 mm. In [20] the tip error was 0.8 and 0.4 mm for a kinematics-based and for a mechanics-based model, respectively and in [9], the error is no better than 0.6 mm. It should be noted that these models make use of model fitting in order to find the model parameters. In our approach, they are independently measured.

The model only requires as input the tissue stiffness and the force applied at the needle tip. When these parameters can be obtained using tissue characterization, the model can be used for both off line and on line path planning. Ultrasound

(a) Measured versus estimated tip force from image feedback



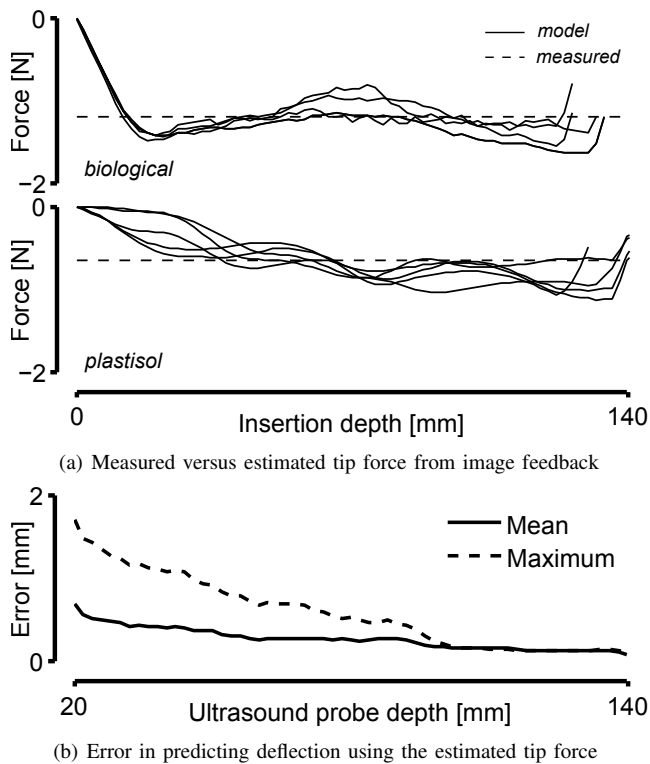(b) Error in predicting deflection using the estimated tip force

Fig. 6. Estimated tip force using image feedback. In (a) the estimated and measured cutting force for biological and plastisol tissues is shown. In (b) the error in predicting needle tip deflection as a function of the depth where the ultrasound probe stops (for biological tissue only) is plotted.

image feedback can also be used to update the tissue cutting force in real time. The ultrasound probe follows the needle tip up to a certain depth and stops. The estimated tip force is then used to predict future deflection of the needle with an average maximum error of less than 1 mm as long as the probe stops at a depth of 55 mm or higher. This is particularly useful in practical conditions, as model parameters are difficult to obtain for needles inserted in tissue *in-vivo*. Furthermore, the method limits the motion of the ultrasound probe to avoid complications of tissue deformation.

Thanks to the current processing time of 0.6 milliseconds, the proposed method can be used in future work to implement a real-time needle steering algorithm.

## REFERENCES

[1] S. DiMaio and S. Salcudean, "Needle insertion modeling and simulation," *Robotics and Automation, IEEE Transactions on*, vol. 19, no. 5, pp. 864–875, Oct 2003.

[2] A. M. Okamura, C. Simone, and M. Leary, "Force modeling for needle insertion into soft tissue," *Biomedical Engineering, IEEE Transactions on*, vol. 51, no. 10, pp. 1707–1716, 2004.

[3] R. J. Webster, J. S. Kim, N. J. Cowan, G. S. Chirikjian, and A. M. Okamura, "Nonholonomic modeling of needle steering," *The International Journal of Robotics Research*, vol. 25, no. 5-6, pp. 509–525, 2006.

[4] G. J. Vrooijink, M. Abayazid, S. Patil, R. Alterovitz, and S. Misra, "Needle path planning and steering in a three-dimensional non-static environment using two-dimensional ultrasound images," *The International Journal of Robotics Research*, p. 0278364914526627, 2014.

[5] N. Abolhassani, R. Patel, and M. Moallem, "Needle insertion into soft tissue: A survey," *Medical engineering & physics*, vol. 29, no. 4, pp. 413–431, 2007.

[6] S. P. DiMaio and S. E. Salcudean, "Interactive simulation of needle insertion models," *Biomedical Engineering, IEEE Transactions on*, vol. 52, no. 7, pp. 1167–1179, 2005.

[7] M. Khadem, B. Fallahi, C. Rossa, R. Sloboda, N. Usmani, and M. Tavakoli, "A mechanics-based model for simulation and control of flexible needle insertion in soft tissue," in *Robotics and Automation, 2015 IEEE International Conference on*, May 2015, pp. 2264–2269.

[8] R. J. Roesthuis, Y. R. van Veen, A. Jahya, and S. Misra, "Mechanics of needle-tissue interaction," in *Intelligent Robots and Systems (IROS), 2011 IEEE/RSJ International Conference on*. IEEE, 2011, pp. 2557–2563.

[9] S. Misra, K. B. Reed, B. W. Schafer, K. Ramesh, and A. M. Okamura, "Mechanics of flexible needles robotically steered through soft tissue," *The International journal of robotics research*, 2010.

[10] T. Lehmann, C. Rossa, N. Usmani, R. Sloboda, and M. Tavakoli, "A virtual sensor for needle deflection estimation during soft-tissue needle insertion," in *Robotics and Automation, 2015 IEEE International Conference on*. IEEE, 2015, pp. 1217–1222.

[11] R. Alterovitz, A. Lim, K. Goldberg, G. S. Chirikjian, and A. M. Okamura, "Steering flexible needles under markov motion uncertainty," in *Intelligent Robots and Systems, 2005.(IROS 2005). 2005 IEEE/RSJ International Conference on*. IEEE, 2005, pp. 1570–1575.

[12] R. Alterovitz, K. Goldberg, and A. Okamura, "Planning for steerable bevel-tip needle insertion through 2d soft tissue with obstacles," in *Robotics and Automation, 2005. ICRA 2005. Proceedings of the 2005 IEEE International Conference on*, April 2005, pp. 1640–1645.

[13] O. Goksel, S. E. Salcudean, and S. P. Dimaio, "3d simulation of needle-tissue interaction with application to prostate brachytherapy," *Computer Aided Surgery*, vol. 11, no. 6, pp. 279–288, 2006.

[14] M. Waine, C. Rossa, R. Sloboda, N. Usmani, and M. Tavakoli, "3d shape visualization of curved needles in tissue from 2d ultrasound images using ransac," in *Robotics and Automation (ICRA), 2015 IEEE International Conference on*, May 2015, pp. 4723–4728.

[15] R. C. Susil, K. Camphausen, P. Choyke, E. R. McVeigh, G. S. Gustafson, H. Ning, R. W. Miller, E. Atalar, C. N. Coleman, and C. Ménard, "System for prostate brachytherapy and biopsy in a standard 1.5 t mri scanner," *Magnetic Resonance in Medicine*, vol. 52, no. 3, pp. 683–687, 2004.

[16] Z. Neubach and M. Shoham, "Ultrasound-guided robot for flexible needle steering," *Biomedical Engineering, IEEE Transactions on*, vol. 57, no. 4, pp. 799–805, 2010.

[17] V. Kallem and N. J. Cowan, "Image-guided control of flexible bevel-tip needles," in *Robotics and Automation, 2007 IEEE International Conference on*. IEEE, 2007, pp. 3015–3020.

[18] Y. Kobayashi, A. Onishi, H. Watanabe, T. Hoshi, K. Kawamura, M. Hashizume, and M. G. Fujie, "Development of an integrated needle insertion system with image guidance and deformation simulation," *Computerized Medical Imaging and Graphics*, vol. 34, no. 1, pp. 9–18, 2010.

[19] P. Moreira and S. Misra, "Biomechanics-based curvature estimation for ultrasound-guided flexible needle steering in biological tissues," *Annals of Biomedical Engineering*, pp. 1–11, 2014.

[20] M. Abayazid, R. J. Roesthuis, R. Reilink, and S. Misra, "Integrating deflection models and image feedback for real-time flexible needle steering," *Robotics, IEEE Transactions on*, vol. 29, no. 2, pp. 542–553, 2013.

[21] P. Yan, J. C. Cheeseborough, and K. C. Chao, "Automatic shape-based level set segmentation for needle tracking in 3-d trus-guided prostate brachytherapy," *Ultrasound in medicine & biology*, vol. 38, no. 9, pp. 1626–1636, 2012.

[22] M. Lachaine and T. Falco, "Intrafractional prostate motion management with the clarity autoscan system," *Med. Phys. Int*, vol. 1, no. 1, pp. 72–80, 2013.

[23] G. Genta, *Vibration dynamics and control*. Springer, 2009.

[24] R. Bhat, "Natural frequencies of rectangular plates using characteristic orthogonal polynomials in rayleigh-ritz method," *Journal of Sound and Vibration*, vol. 102, no. 4, pp. 493–499, 1985.